

Exploring the influence of FIB processing and SEM imaging on solid-state electrolytes

Ziming Ding, Yushu Tang, Venkata Sai Kiran Chakravadhanula, Qianli Ma, Frank Tietz, Yuting Dai, Torsten Scherer, Christian Kübel*

Ziming Ding, Institute of Nanotechnology (INT), Karlsruhe Institute of Technology (KIT), 76344 Eggenstein-Leopoldshafen, Germany; Technische Universität Darmstadt, 64289 Darmstadt, Germany. [+4972160834346](tel:+4972160834346) ziming.dng@kit.edu

Yushu Tang, Institute of Nanotechnology (INT), Karlsruhe Institute of Technology (KIT), 76344 Eggenstein-Leopoldshafen, Germany; [+4972160828932](tel:+4972160828932) yushu.tang@kit.edu

Venkata Sai Kiran Chakravadhanula, cvsikiran@gmail.com

Qianli Ma, Forschungszentrum Jülich GmbH, Institute of Energy and Climate Research, Materials Synthesis and Processing (IEK-1), 52425 Jülich, Germany; [+492461/61-9705](tel:+492461619705) g.ma@fz-juelich.de

Frank Tietz, Forschungszentrum Jülich GmbH, Institute of Energy and Climate Research, Materials Synthesis and Processing (IEK-1), 52425 Jülich, Germany; [+492461/61-5007](tel:+492461615007) f.tietz@fz-juelich.de

Yuting Dai, Institute of Nanotechnology (INT) and Helmholtz Institut Ulm (HIU), Karlsruhe Institute of Technology (KIT), 76344 Eggenstein-Leopoldshafen, Germany; Technische Universität Darmstadt, 64289 Darmstadt; [+4972160828932](tel:+4972160828932) yuting.dai@partner.kit.edu

Torsten Scherer, Institute of Nanotechnology (INT), Karlsruhe Institute of Technology (KIT), 76344 Eggenstein-Leopoldshafen, Germany; [+4972160828365](tel:+4972160828365) torsten.scherer@kit.edu

Christian Kübel*, Institute of Nanotechnology (INT), Helmholtz Institute Ulm (HIU), and Karlsruhe Nano Micro Facility (KNMF), Karlsruhe Institute of Technology (KIT), 76344

Eggenstein-Leopoldshafen, Germany; Technische Universität Darmstadt, 64289 Darmstadt;
[+4972160828970 christian.kuebel@kit.edu](mailto:christian.kuebel@kit.edu)

Keywords: focused ion beam; scanning electron microscopy; beam damage; Au-coating; cryogenic condition; solid-state electrolyte.

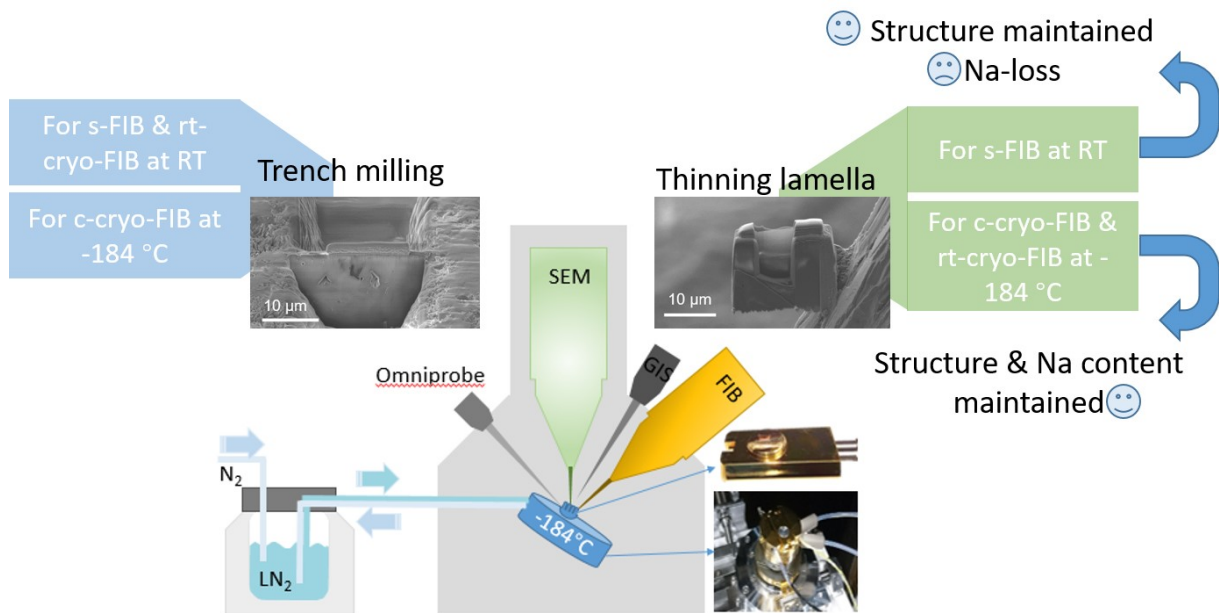
Total number of pages: 22

Total number of figures: 8

Abstract

Performing reliable preparation of TEM samples is the necessary basis for a meaningful investigation by *ex-situ* and even more so by *in-situ* TEM techniques, but it is challenging using materials that are sensitive to electron-beam irradiation. FIB is currently the most commonly employed technique for a targeted preparation, but the structural modifications induced during FIB preparation are not fully understood for a number of materials. Here, we have investigated the impact of both the electron and the Ga⁺ ion beam on insulating solid-state electrolytes (LiPON, BASE and NaSICON) and observed significant Li/Na whisker growth induced by both the electron and ion beam already at fairly low dose leading to a significant change in the chemical composition. The metal whisker growth is presumably mainly due to surface charging which can be reduced by coating with a gold layer or preparation at cryogenic conditions as efficient approaches to stabilize the solid electrolyte for SEM imaging and TEM sample preparation. Details on the different preparation approaches, the acceleration voltage dependence and the induced chemical and morphological changes are reported.

Graphical abstract



Introduction

All-solid-state batteries (ASSBs) have a promising application potential due to their high safety, in part due to the non-flammable nature of the solid-state electrolytes (SSEs) and their good mechanical stability, the potential for fast charging/discharging, and the high energy density with metallic anodes. [1-3] However, solid-solid interfaces, both in between electrode and electrolyte as well as within, are still a major bottleneck for ASSBs to enter the market. [4] To understand and visualize the solid-solid interfaces, electron microscopy including scanning electron microscopy (SEM) and transmission electron microscopy (TEM) coupled with electron and X-ray spectroscopy are some of the most advanced characterization techniques to understand their morphology, structure, composition, and oxidation state either during static imaging or dynamically at high resolution down to the atomic scale. [5] However, accessing the interfaces and producing electron-transparent specimens of the region of interest for TEM analysis without altering or damaging their structure is one of the obstacles to discover the story of materials degradation during

battery cycling. A variety of approaches for SEM and TEM sample preparation of different electrode materials [6-8] and solid-solid interfaces [9, 10] have been reported in the literature mainly including mechanical methods (e.g. using ultramicrotome [6] and diamond-tipped pen [10]), broad ion beam polishing (e.g. ion slicer [8, 11]) and focused ion beam (FIB) [12-14] as well as the combination of FIB and ultramicrotomy [7]. Mechanical and broad ion beam polishing methods are preferred for preparation of samples with large dimensions, but can be challenging for brittle and air-sensitive materials such as oxide solid electrolytes [9] or for a targeted preparation from a specific area. Alternatively, FIB-based TEM sample preparation techniques are currently probably the most employed approaches and have been used to look at a variety of SSEs such as LIPON- [15], oxide- [16] and sulfide-based [17] lithium and fluoride [18] fast ion conductors. In particular, for the preparation of samples suitable for *in-situ* TEM investigation of SSEs, FIB-based preparation techniques are the standard approach, especially for micro-electro-mechanical system (MEMS) based *in-situ* setups [18], but also for scanning tunneling microscopy-based *in-situ* transmission electron microscopy (STM-TEM) approaches [15]. While the impact of electron and ion beams on the structure and defects in semiconductor materials and devices have been extensively investigated, e.g. the influence of acceleration voltage, dose and dose rate, as well as various scanning strategies [19, 20], the influence of FIB processing including SEM imaging on solid electrolytes is less well explored.

In addition to the well-known air and moisture sensitivity of many battery materials [21] and charging problems of SSEs due to their low electric conductivity [22, 23], a fundamental issue are inherent damages by electron and ion beam on the structure, chemistry and oxidation state of battery materials. [24] Understanding and mitigating those challenges is essential for TEM analysis to investigate the real solid-solid interfaces in batteries. This becomes even

more critical for *in-situ* investigations, where it is often unknown how preparation induced changes affects the electrochemical processes to be studied. For example, Lee et al. showed that metallic lithium can be protected from morphological and significant chemical changes by performing the FIB sample processing under cryogenic conditions. [25] This enabled the investigation of the interfacial evolution between Li and a SSE during electrochemical cycling of a cross-section through a compressed ASSB.

Here we report on the morphological, structural and chemical changes of three common SSEs, LiPON, Na-beta''-alumina (BASE), and Na_{3.4}Si_{2.4}Zr₂P_{0.6}O₁₂ (NaSICON) induced by SEM imaging and FIB processing and introduce an efficient cryo-FIB approach to prevent significant changes during TEM sample preparation to enable reliable *in-situ* and *ex-situ* analysis of these materials in the TEM.

Materials

Three common oxide-based SSEs have been investigated: pellets of commercial Na-beta''-alumina (BASE) (Ionotec Ltd.) and Na_{3.4}Si_{2.4}Zr₂P_{0.6}O₁₂ (NaSICON) prepared according to [26] as examples for Na⁺ ion conductors as well as LiPON thin films (prepared by the group of Wolfgang Jägermann at Technical University Darmstadt) [27] as an example for a Li⁺ ion conductors used in Li ASSBs.

Methods

Standard and cryogenic FIB sample preparation have been performed using a Strata 400 S (FEI Company) dual-beam FIB and an Auriga 60 cross beam FIB (Zeiss). In addition to the

cryogenic FIB process, a self-made stub with specimen and TEM grid position was made for the liquid nitrogen cooling stage (Gatan Inc.) as shown in **Figure 1**. For the BASE and NaSICON preparation, the samples were coated with a nominally 100 nm thick Au layer in a sputter coater (Quantum Design GmbH) on the SSE pellets and the silver paste was used to connect the surface of specimens and the SEM stubs to improve the electric conductivity for SEM/FIB imaging. Afterwards we performed both standard (here labeled s-FIB) as well as cryogenic FIB processing as shown in **Figure 1**. The preparation labeled s-FIB follows standard FIB procedures[28] at room temperature (RT). Pt was first deposited using the electron beam with an acceleration voltage of 5 kV and current of 1.6 nA. The total electron dose for the deposition was around $8.1 \times 10^8 \text{ e/nm}^2$. Afterwards Pt deposition performed by FIB with a total dose of around $1.4 \times 10^4 \text{ Ga}^+/\text{nm}^2$. The trench milling and cutting of the lamella from the bulk was carried out with a total ion dose of $1.7 \times 10^5 \text{ Ga}^+/\text{nm}^2$ at 30 kV and a current of 9.3 nA to obtain a lamella with a thickness of around 2.5 μm . The lamella was transferred to the TEM grid with a micromanipulator. The lift-out and transfer process required around 1200 e/nm^2 for SEM imaging and $400 \text{ Ga}^+/\text{nm}^2$ for attaching/removing the micromanipulator. For the final thinning and polishing, a dose of around $6.2 \times 10^4 \text{ Ga}^+/\text{nm}^2$ at 30 kV was used. At the end, to remove redeposited material and Ga ions from the surface of the TEM lamella, the specimen was briefly cleaned using a 5 kV ion beam. SEM imaging to support the milling and polishing procedures (including intermittent viewing and patterning) was conducted at 5 kV and with a current of 1.6 nA and a viewing frequency of 1 Hz. The final dose was estimated to be 1200 e/nm^2 for the milling and polishing. The detailed parameters are listed in **Table 1**.

The preparation labeled c-cryo-FIB was performed analogously, but both the trench milling as well as the final polishing were performed at cryogenic conditions ($-184 \text{ }^\circ\text{C}$) using a liquid

nitrogen cooling stage (Gatan Inc.). For the sample labeled rt-cryo-FIB only the final polishing was performed at -184 °C, but the trench milling was performed at room temperature. In all cases, the doses and dose rates were similar. In all cases, the micromanipulator (Omniprobe 200 at Strata, Omniprobe 400 at Auriga) was kept at room temperature and the gas injection needles (GIS) were heated to 80 °C. This allowed for cryogenic preparation of lift-out samples, using a regular FIB only equipped with a cryogenic stage.

Typically, mainly the ion beam effects are considered to understand damage induced during FIB preparation. However, also the electron beam in the SEM can lead to significant changes of materials. [29, 30] To investigate electron beam effects in the SEM for SSEs in more detail, we performed a systematic series of dose experiments at various acceleration voltages (0.5-30 kV) using the SEM column inside the Strata 400 dual beam FIB for LiPON thin films as well as the BASE pellet sample. For this analysis, we simply evaluated the morphological changes in the sample with increasing dose during continuous imaging at a fixed magnification.

A probe-corrected Themis 300 TEM (ThermoFischer Scientific) operated at 300 kV was used for TEM analysis of the (cryo) FIB prepared samples. The electron beam diameter was nominally 170 pm with a convergence angle of 30 mrad and a screen current of 70 pA. High-angle annular dark-field scanning transmission electron microscopy (HAADF-STEM) imaging with energy-dispersive X-ray spectroscopy (EDS) (Super-X EDS detector) and electron diffraction were used to characterize the composition and microstructure of the TEM lamellas prepared by the different FIB processes. The dose for one EDS map was around 2000 e/nm². The Brown-Powell ionization cross-section model was used for the EDS quantification after second order multi-polynomial modelling and subtraction of the background; the sample thickness and density were estimated for adsorption correction. Prior to TEM characterization, the TEM lamellas were cleaned by an argon-oxygen plasma

using a 1070 Plasma Cleaner (Fischione Inc.) to remove the carbon compounds adsorbed on the surface. The FIB-processed SSE specimens were kept in a glove box for intermediate storage due to their sensitivity to humidity. Long-term exposure to air leads to a loss of Na from the SSE. [31] However, the short transfer from the glove box to the TEM through air turned out not to be critical.

Results and Discussion

During standard (*s*-FIB) TEM preparation of both BASE and NaSICON, we noticed whiskers growing from the frame of the lamella and the thinned region as highlighted in **Figure 2a & c**. The whiskers on the frame grow as the thinning of the central area progresses as shown in **Figure S1**. In the thinned region, this growth was not as obvious as further thinning partially removed the developing whiskers. However, whiskers tend to develop again at the same position after removing them by further thinning. Based on the fairly well-defined polyhedral shape, we assume that the whiskers were originally metallic Na, which oxidized during sample transfer into the TEM. [32] Despite the sodium extraction from the SSE, the basic crystalline structure of the SSEs is well maintained as can be seen from the electron diffraction data (**Figure 2b & d**), which is in excellent agreement with the NaSICON and BASE structure. We expect that the specific physical properties of the SSEs, in particular the high mobility of Na⁺ ions and the extremely low electronic conductivity contribute to the development of Na whiskers during the ion-polishing procedure, while this effect is typically not observed in electrode materials. Radiolysis of ceramics typically leads to a displacement of atoms in the anion sublattice, [33] which further leads to a loss of oxygen (in case of oxide-based ceramics)[30] and ultimately to a damage of the crystalline lattice [33, 34].

Nevertheless, even during our room temperature sample preparation, the damage to the crystal lattice was apparently not significant enough to see noticeable changes in the diffraction patterns. However, the sodium located in between the cation sublattice is highly mobile in SSEs. In analogy to the electric field-induced damage mechanism suggested by Jiang et al. in STEM, [22, 23] we suggest that the electric field induces Na^+ ion migration during FIB processing and SEM imaging as well. The sodium ions in the bulk are driven to migrate either directly in the electric field gradient of the ion/electron beam as well as towards the sample surface due to the electric field developing in the insulating sample and by the accumulation of surface charges from the SEM or FIB imaging. Once at the surface, the sodium ions can be reduced by surface electrons. This fits to the nucleation and growth of Na whiskers observed mostly at the edges of the thicker frame of the TEM lamella, where the strongest charging is expected and a rich Na reservoir is present in close vicinity. In contrast, during the trench milling procedure, we barely observed growth of Na whiskers on the surface of the specimen even though much larger ion doses have been employed. This is presumably related to the thick gold coating on the specimen surface, which is further connected via silver paste to the ground thus providing good electrical contact, preventing significant charge accumulation at the surface both for the bulk specimen as well as the (still thick and well connected) TEM lamella. [35] Therefore, the main driving force for sodium ion migration and sodium whisker growth is not present during this step.

To understand the influence of the standard FIB process on the SSEs, TEM characterization of the s-FIB fabricated lamellas has been performed. Surprisingly, the selected area electron diffraction (SAED) pattern of the BASE TEM lamella (**Figure 2b**) can be clearly indexed as [110] zone axis of Na-beta''-alumina (based on ICSD_200990) (**Table S1**). This indicates that the typical layer structure of the BASE material is maintained after the s-FIB process. Moreover,

the lattice parameters are not strongly affected by the sodium loss, which is in agreement with observations during synthesis of BASE with various sodium content [36]. Similarly, the nano-beam electron diffraction (NBED) of NaSICON (**Figure 2d**) can be indexed well as $[\bar{1}01]$ zone axis of the monoclinic NaSICON structure [26] (based on ICSD_473). This indicates that the sodium whisker growth during FIB thinning does not significantly influence the crystal structure of the SSEs and the sodium ion transport path is presumably maintained after ion beam milling and polishing. A slight oxygen loss reported previously for various other oxides [29] and ceramics [30] can presumably be quickly recovered during the transfer of the TEM lamella from the FIB to the TEM [29] further helping to recover/maintain the sodium ion transport paths.

At higher magnification, HAADF-STEM images and low dose EDS elemental maps of BASE (**Figure 3a - d**) show a reduced Al signal indicating a thinner region compared to the adjacent grains, suggesting that this region was next to a void prior to specimen polishing, while small particles can be seen in the vicinity of voids and grain boundaries. Looking at the corresponding Na map, the small particles can be identified as Na (oxide), which originated from Na whiskers after the thinning procedure. This indicates that the Na whiskers preferentially grow at voids and grain boundaries during the thinning procedure. This has also been observed during *in-situ* TEM studies looking at the influence of grain boundaries on sodium ion migration. [37] **Figure 3a** also shows a triple boundary (orange arrow), which presumably turned into a crack after thinning. This can be attributed to strain induced by the growth of sodium whiskers at the triple boundary.[37, 38] This suggests that the growth of the Na whiskers may also lead to some microstructural changes during thinning. Similar to the s-FIB processed BASE material, Na was also found in the vicinity of voids/gaps of s-FIB processed NaSICON TEM lamella as indicated by the white arrow in **Figures 3e and 3f**. In

addition, local Na fluctuations are also visible in **Figures 3e-f and S2**. In the vicinity of the Au coating layer, a significantly reduced sodium content was observed in some NaSICON specimens due to FIB induced alloying of sodium and gold.

Although the crystal structure of the BASE and NaSICON material is maintained after the s-FIB TEM sample preparation, the Na whiskers growing from the frame of the lamella have a strong influence on the Na content of the thinned area due to the high mobility of Na⁺ ions in the SSEs. The Na content of the thinned area is critical for the application of the SSE due to the altered ionic conductivity, activation energy and the driving force for ion migration. This, in turn, will affect *in-situ* TEM experiments of oxide-SSE-based micro-/nano-batteries.[36, 39] STEM-EDS analysis of the thinned area of the BASE and NaSICON lamella (**Figure 4a & b**) reveals that the Na content of the thinned lamella is significantly reduced when looking at the Al:Na (BASE) and Si:Na (NaSICON) ratio. The atomic ratio between Al and Na of the bulk BASE is 1:0.16, whereas in the s-FIB fabricated BASE lamella it is reduced to 1:0.06. The atomic ratio of Si and Na in bulk NaSICON is 1:1.42,[26] whereas in the s-FIB fabricated NaSICON it is reduced to 1:1.11. This indicates that around 60% of Na is lost in the thinned BASE lamella due to Na whiskers growth induced by the ion beam and around 20% Na is lost in the thinned NaSICON lamella.

As the crystal lattice of both BASE and NaSICON is maintained during FIB preparation and the most critical change during s-FIB fabrication is Na loss due to Na migration, cryogenic preparation should help to maintain the chemical composition by decreasing the Na⁺ ion mobility. Ideally, the whole preparation should be performed under cryogenic conditions, but with a standard FIB this is not possible. Compared to the necessary ion dose for the trench milling and lamella thinning, the cut-off of the lamella during the lift-out process requires significantly lower dose. Therefore, the lift-out process is expected to have only a

small influence on the overall lamella preparation. Hence, in this work, we used a FIB system equipped with a liquid nitrogen cooling stage to maintain cryogenic condition for trench milling and thinning (c-cryo-FIB), whereas the Pt electron and ion deposition as well as the lift-out procedures were carried out at room temperature. Since we did not notice Na wire growth during trench milling, we further tried to simplify the fabrication procedures by applying cryogenic condition only during TEM lamella thinning and polishing (rt-cryo-FIB). With this approach, we did not observe any Na whiskers forming during the cryogenic thinning procedure of both SSEs (**Figure S3**). A clean surface and uniform Na distribution were observed as shown in **Figure 5**. Furthermore, the average Na content of the lamellas fabricated by c-cryo-FIB and rt-cryo-FIB have been determined by EDS (**Figure 4**). With both cryogenic milling and polishing procedures, the Na to Al atomic ratio was improved to 1: 6.5, which is close to the as-prepared bulk BASE composition, and after rt-cryo-FIB the ratio was still around 1: 6.6, close to the bulk composition. Similarly, in NaSICON, the Na to Si atomic ratio is at the same level as the as-prepared bulk NaSICON already when using cryogenic polishing. This indicates that the cryogenic conditions prevent a Na loss in the processed region. In addition, it suggests that controlling the cryogenic polishing during FIB processing is an efficient way to prepare TEM lamella of oxide SSEs.

Beside the ion beam induced damage during FIB preparation, herein, we also investigated the material changes induced by the electron beam, which is necessary for viewing and patterning in SEM/FIB. It is widely accepted that charging effects occur in non-conductive materials leading to a buildup of electric fields due to the accumulated surface electrons during SEM imaging. [35, 40] Moreover, STEM imaging in the TEM is already known to facilitate Li^+ ion diffusion and phase separation, which is induced by the gradient of electric field in the material.[41] However, there is only limited information on the influence of the

electron beam on the SSEs in the SEM. Therefore, we have explored morphological changes of SSEs in the SEM depending on dose and acceleration voltage of the electron beam.

During SEM imaging of LiPON thin films, we noticed distinct morphological changes in the material with increasing dose. Starting at a dose as low as 22 e/nm^2 at 2 kV acceleration voltage, first morphological changes appeared as small bright spots randomly distributed on the previously uniform thin film surface (**Figure 6**). With increasing dose, these features disappeared gradually (video supplementary information) and turned dark as shown in **Figure 6c**. This morphological evolution is illustrated schematically in **Figure 6f**. As a potential explanation for this behavior, we propose surface charging of the LiPON thin film due to the limited electrical conductivity inducing Li^+ migration to the surface, where the Li^+ ions are reduced to Li. The thin Li deposits might react with residual air/water in the FIB chamber and/or will be damaged by the continuous electron beam illumination leading to the dark features observed during SEM imaging. In addition, the dose applied to the sample is at a level, where previous studies indicated first damage in the oxide structure to appear,[29, 30] which might also be responsible for the observed changes.

With further increasing dose, additional morphological changes become visible (**Figure 6c/d**). First, larger spherical particles appear (white arrow in **Figure 6c**), followed by whisker-growth from the substrate at one edge of the particles (orange arrow in **Figure 6d**). The whiskers are assumed to be metallic Li due to their well-defined polyhedral-like shape with characteristic faceting angles of around 120° . The spherical particles and the whiskers always start to grow at the left boundary of the scanning area followed by the right, top/bottom edge of the scanning and only at much higher dose they appear in the middle of the scanning area (see supplementary movie) at a dose of 2300 e/nm^2 . Surface charging leads to the largest electric field gradient at the boundary between the scanned and the surrounding

area followed by preferential Li whisker growth there. The initial start of the growth on the left side of the scanned area (marked with the orange dashed rectangle in **Figure 6e**) can be explained by the slightly higher dose applied there due to the fly-back time of the SEM beam during scanning. Both, during the growth and at lower magnification (**Figure 6e**), it becomes obvious that the whiskers grow pointing away from the edge of the scan frame, presumably due to the orientation of the electric field gradient. Only on the side marked in **Figure 6e** the whiskers grow to the left pointing away from the frame as the actual illuminated region starts there. Another contribution to the observed directed Li dendrite growth could also be the number of surface charges present, which would lead to faster Li reduction and higher growth speed in locations with higher amount of surface charges.

In addition to the dependence on dosage, the influence of the acceleration voltage was also investigated as shown in **Figure 7**. Applying the same final dose of 3500 e/nm^2 , SEM images of LiPON were acquired at different acceleration voltages. At low voltages of 0.5 and 1 kV, no whisker growth was observed, but only some surface changes built up, probably due to slight carbon contamination. At intermediate acceleration voltages of 2 kV, 3 kV, 5 kV, and 10 kV, clear whisker growth was observed. The whisker density decreased and their size increased with increasing acceleration voltage in this range. This is presumably related to the distribution of surface electrons and the involved excitation volume. At low acceleration voltages (0.5 kV and 1 kV), surface charging is leading to limited electric field buildup to induce Li^+ ion migration. However, increasing acceleration voltages lead to an increase in the electron penetration depth and interaction volume with increased surface charging. Consequently, an increasing number of Li^+ ions are affected to produce Li whiskers. The density changes are presumably a consequence of difference in the nucleation and diffusion rates with increasing high tension. At higher acceleration voltages of 15 kV, 20 kV, and 30 kV

the morphological changes became less pronounced. A potential contribution could be the increasingly likely surface sputtering of Li at higher acceleration voltages, thus removing the Li growing on the surface. The threshold voltage for surface sputtering of Li has been estimated to be around 5-9 kV [42], fitting to the significantly reduce observation of Li wires above 10 kV acceleration voltage. Based on the morphological evolution at different acceleration voltages, extremely low acceleration voltage of 0.5 kV and 1 kV are the best conditions for SEM imaging of LiPON during FIB preparation to reduce electron beam-induced damages.

As an alternative approach, a metal coating is a well-known method to minimize the charging effect in the SEM.[35] Therefore, in this work, the BASE and NaSICON pellets were coated with Au for the TEM sample preparation. Here, we compared the behavior of Au-coated and uncoated BASE pellets using the same dose condition as before (**Figure 8**). Without an Au coating, whiskers started to appear at a dose of around 600 e/nm^2 (white arrows in **Figure 8b**) and more whiskers grew around the edge of the scan area after a dose of around 1200 e/nm^2 (**Figure 8c**). However, the Au-coated sample did not show any whisker growth under the same dose condition (**Figure 8d-f**) and even at a much higher dose of around 60000 e/nm^2 no whisker growth was observed (**Figure S4**). The suppression of whisker growth during SEM imaging of the Au-coated specimen is another indication that the whisker growth is related to surface charges and the resulting electric field. In turn, the Au coating is an efficient protection preventing metal ion migration in the SEM.

Conclusion

We explored the influence of FIB processing and SEM imaging on oxide SSEs during imaging and TEM sample preparation. Li/Na whiskers grew from the SSE surface, induced by both the electron as well as the ion beam. We proposed that the local electric fields generated by the electron/ion beam and, more dominant, the charging of the insulating SSE samples is the driving force for Li/Na migration. When good electrical contact of the SSE is maintained, no significant Na loss was observed, but the final thinning and polishing procedure was critical. With typical room temperature FIB preparation, this resulted in a Na loss of around 60% in case of BASE and 20% in case of NaSICON. Nevertheless, the crystal structure of both SSEs were maintained during FIB preparation without noticeable changes in lattice parameters. To reduce Na migration during TEM sample preparation, cryogenic preparation with liquid N₂ cooling was successful, resulting in TEM samples with essentially maintained nominal composition. Even if only the final thinning and polishing was performed with liquid N₂ cooling, the preparation of TEM samples without noticeable changes was successful. This is a very efficient way to prepare sensitive samples.

Not only the Ga⁺ ion beam is changing the sample, but already SEM imaging can induce significant Li⁺/Na⁺ ion migration in SSEs. Whisker growth was observed during SEM imaging both for LiPON thin films and BASE ceramics. The damage is dependent on acceleration voltage and results in significant whisker growth between 2 and 10 kV acceleration voltages. The observed morphological changes are also in agreement with surface charging as the main driving force for ion migration. Applying a protective layer of gold to strongly reduce surface charging, thus efficiently reduces the damage during SEM imaging and thus helps during SEM characterization as well as for a good TEM sample preparation by FIB.

Acknowledgments

This work contributes to the research performed at CELEST (Center for Electrochemical Energy Storage Ulm-Karlsruhe) and was funded by the German Research Foundation (DFG) under Project ID 390874152 (POLiS Cluster of Excellence). Yuting Dai acknowledges financial support from the China Scholarship Council (CSC). We acknowledge the support of Mr. Till Ortmann for NaSICON material. We acknowledge Mr. M. Motzko and R. Hausbrand from TU Darmstadt for providing LiPON thin film. We acknowledge the Karlsruhe Nano Micro Facility (KNMFi) at KIT for providing TEM and FIB access.

Data Statement

The original data is available at KITOpen through the DOI: [10.5445/IR/1000152787](https://doi.org/10.5445/IR/1000152787)

References

1. Shen, Y., et al., *Unlocking the Energy Capabilities of Lithium Metal Electrode with Solid-State Electrolytes*. *Joule*, 2018. **2**(9): p. 1674-1689.
2. Varzi, A., et al., *Challenges and prospects of the role of solid electrolytes in the revitalization of lithium metal batteries*. *Journal of Materials Chemistry A*, 2016. **4**(44): p. 17251-17259.
3. Zhao, C., et al., *Solid-State Sodium Batteries*. *Advanced Energy Materials*, 2018. **8**(17).
4. Xu, L., et al., *Interfaces in Solid-State Lithium Batteries*. *Joule*, 2018. **2**(10): p. 1991-2015.
5. Qian, D., et al., *Advanced analytical electron microscopy for lithium-ion batteries*. *NPG Asia Materials*, 2015. **7**(6): p. e193-e193.
6. Zhang, H., C. Wang, and G. Zhou, *Ultra-Microtome for the Preparation of TEM Specimens from Battery Cathodes*. *Microsc Microanal*, 2020. **26**(5): p. 867-877.

7. Chae, J.E., et al., *Transmission Electron Microscope Specimen Preparation of Si-Based Anode Materials for Li-Ion Battery by Using Focused Ion Beam and Ultramicrotome*. Applied Microscopy, 2018. **48**(2): p. 49-53.
8. Park, J.S., et al., *TEM sample preparation of microsized LiMn2O4 powder using an ion slicer*. Appl Microsc, 2021. **51**(1): p. 19.
9. López, I., et al., *A critical discussion on the analysis of buried interfaces in Li solid-state batteries. Ex situ and in situ/operando studies*. Journal of Materials Chemistry A, 2021. **9**(45): p. 25341-25368.
10. Song, X., et al., *A special TEM Li-ion battery sample preparation and application technique for investigating the nano structural properties of the SEI in lithium ion batteries*. MRS Advances, 2020. **5**(27): p. 1415-1421.
11. Masuda, H., et al., *Internal potential mapping of charged solid-state-lithium ion batteries using in situ Kelvin probe force microscopy*. Nanoscale, 2017. **9**(2): p. 893-898.
12. Lee, J.Z., et al., *Focused Ion Beam Fabrication of LiPON-based Solid-state Lithium-ion Nanobatteries for In Situ Testing*. J Vis Exp, 2018(133).
13. Walther, F., et al., *Visualization of the Interfacial Decomposition of Composite Cathodes in Argyrodite-Based All-Solid-State Batteries Using Time-of-Flight Secondary-Ion Mass Spectrometry*. Chemistry of Materials, 2019. **31**(10): p. 3745-3755.
14. Walther, F., et al., *Influence of Carbon Additives on the Decomposition Pathways in Cathodes of Lithium Thiophosphate-Based All-Solid-State Batteries*. Chemistry of Materials, 2020. **32**(14): p. 6123-6136.
15. Wang, Z., et al., *In Situ STEM-EELS Observation of Nanoscale Interfacial Phenomena in All-Solid-State Batteries*. Nano Lett, 2016. **16**(6): p. 3760-7.
16. Li, S., et al., *Direct Observation of Defect-Aided Structural Evolution in a Nickel-Rich Layered Cathode*. Angew Chem Int Ed Engl, 2020. **59**(49): p. 22092-22099.

17. Wang, L., et al., *In-situ visualization of the space-charge-layer effect on interfacial lithium-ion transport in all-solid-state batteries*. Nat Commun, 2020. **11**(1): p. 5889.
18. Hammad Fawey, M., et al., *In situ TEM studies of micron-sized all-solid-state fluoride ion batteries: Preparation, prospects, and challenges*. Microsc Res Tech, 2016. **79**(7): p. 615-24.
19. Lotnyk, A., et al., *Focused high- and low-energy ion milling for TEM specimen preparation*. Microelectronics Reliability, 2015. **55**(9-10): p. 2119-2125.
20. Mayer, J., et al., *TEM Sample Preparation and FIB-Induced Damage*. MRS Bulletin, 2011. **32**(5): p. 400-407.
21. Zhao, S., et al., *Fundamental air stability in solid-state electrolytes: principles and solutions*. Materials Chemistry Frontiers, 2021. **5**(20): p. 7452-7466.
22. Jiang, N., *Damage mechanisms in electron microscopy of insulating materials*. Journal of Physics D: Applied Physics, 2013. **46**(30).
23. Jiang, N., *Electron beam damage in oxides: a review*. Rep Prog Phys, 2016. **79**(1): p. 016501.
24. Tietz, F., J. Koepke, and W. Urland, *Analytical investigations of β -Al₂O₃ and β "-Al₂O₃ crystals*. Journal of Crystal Growth, 1992. **118**(3): p. 314-318.
25. Lee, J.Z., et al., *Cryogenic Focused Ion Beam Characterization of Lithium Metal Anodes*. ACS Energy Letters, 2019. **4**(2): p. 489-493.
26. Ma, Q., et al., *Room temperature demonstration of a sodium superionic conductor with grain conductivity in excess of 0.01 S cm⁻¹ and its primary applications in symmetric battery cells*. Journal of Materials Chemistry A, 2019. **7**(13): p. 7766-7776.
27. Hausbrand, R., et al., *Surface and Interface Analysis of LiCoO₂ and LiPON Thin Films by Photoemission: Implications for Li-Ion Batteries*. Zeitschrift für Physikalische Chemie, 2015. **229**(9): p. 1387-1414.
28. Tomus, D. and H.P. Ng, *In situ lift-out dedicated techniques using FIB-SEM system for TEM specimen preparation*. Micron, 2013. **44**: p. 115-9.

29. Neelisetty, K.K., et al., *Electron Beam Effects on Oxide Thin Films—Structure and Electrical Property Correlations*. *Microscopy and Microanalysis*, 2019. **25**(3): p. 592-600.
30. Molinari, A., et al., *Configurable Resistive Response in BaTiO₃ Ferroelectric Memristors via Electron Beam Radiation*. *Advanced Materials*, 2020. **32**(12): p. 1907541.
31. Fertig, M.P., et al., *Humidity-Induced Degradation of Lithium-Stabilized Sodium-Beta Alumina Solid Electrolytes*. *Batteries*, 2022. **8**(9).
32. Geng, L., et al., *In situ imaging the dynamics of sodium metal deposition and stripping*. *Journal of Materials Chemistry A*, 2022. **10**(28): p. 14875-14883.
33. Hobbs, L.W., et al., *Radiation effects in ceramics*. *Journal of Nuclear Materials*, 1994. **216**: p. 291-321.
34. Parajuli, P., et al., *Direct Observation of Electron Beam-Induced Phase Transition in MgCrMnO₄*. *Chemistry of Materials*, 2020. **32**(24): p. 10456-10462.
35. Kim, K.H., et al., *Charging Effects on SEM/SIM Contrast of Metal/Insulator System in Various Metallic Coating Conditions*. *MATERIALS TRANSACTIONS*, 2010. **51**(6): p. 1080-1083.
36. Naqash, S., et al., *Impact of sodium excess on electrical conductivity of Na₃Zr₂Si₂PO₁₂ + x Na₂O ceramics*. *Solid State Ionics*, 2019. **336**: p. 57-66.
37. Ziming Ding, et al., *In-situ TEM observation of Na-filament growth in Na-ion all-solid-state batteries*. in preparation.
38. Liu, Q., et al., *In Situ Observation of Sodium Dendrite Growth and Concurrent Mechanical Property Measurements Using an Environmental Transmission Electron Microscopy–Atomic Force Microscopy (ETEM-AFM) Platform*. *ACS Energy Letters*, 2020. **5**(8): p. 2546-2559.
39. Naqash, S., et al., *Microstructure-conductivity relationship of Na₃Zr₂(SiO₄)₂(PO₄) ceramics*. *Journal of the American Ceramic Society*, 2019. **102**(3): p. 1057-1070.
40. Kanaya, K., et al., *Observations on charging effects of non-conductive and uncoated materials by ion beam pre-bombardment in scanning electron microscopy*. *Micron and Microscopica Acta*, 1992. **23**(3): p. 319-335.

41. Jiang, N., *On the in situ study of Li ion transport in transmission electron microscope*. Journal of Materials Research, 2014. **30**(3): p. 424-428.
42. Egerton, R.F., P. Li, and M. Malac, *Radiation damage in the TEM and SEM*. Micron, 2004. **35**(6): p. 399-409.

Table & Figures

Table 1. Work parameters for the different FIB processing conditions

Table 1. Work parameters for the different FIB processing conditions

Step	FIB process	Working temperature/ °C			Acceleration voltage & beam current	The angle between specimens surface and the ion or electron beam/degree
		s-FIB	c-cryo-FIB	rt-cryo-FIB		
1	Pt deposition	RT			Electron beam: 5kV/1.6nA	0
					Ion beam: 30kV/280pA	52 (strata) 54 (Auriga)
2	Trench milling	RT	-184	RT	Ion beam: 30kV/9.3nA for s-FIB/rt-cryo-FIB & 16nA for c-cryo-FIB	0
3	Lift-out and glue to TEM grid	RT			Electron beam: 5kV/1.6nA	0
					Ion beam: 30kV/280pA	52 (strata) 54 (Auriga)
4	Thinning lamella	RT	-184	-184	Ion beam: 30kV/93pA-430pA for s-FIB & 240 pA for c-cryo-FIB & rt-cryo-FIB	Upside: -1.5 Downside: 1
5	Cleaning surface	RT	-184	-184	Ion beam: 5kV/48pA	Upside: -7 Downside: 1.5

Figure 1. Working procedures of different FIB processes

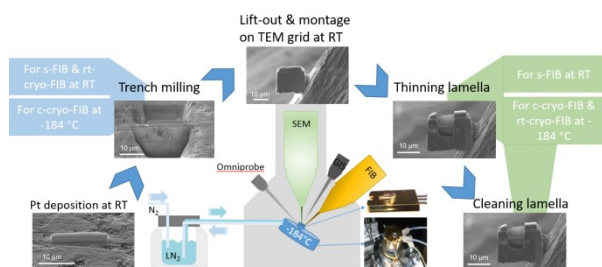


Figure 2. BASE and NaSICON fabricated by s-FIB; a. SEM image of the BASE during the thinning procedure; b. selected area electron diffraction (SAED) of BASE; c. SEM image of NaSICON during the thinning procedure; d. nano-beam electron diffraction (NBED) of NaSICON.

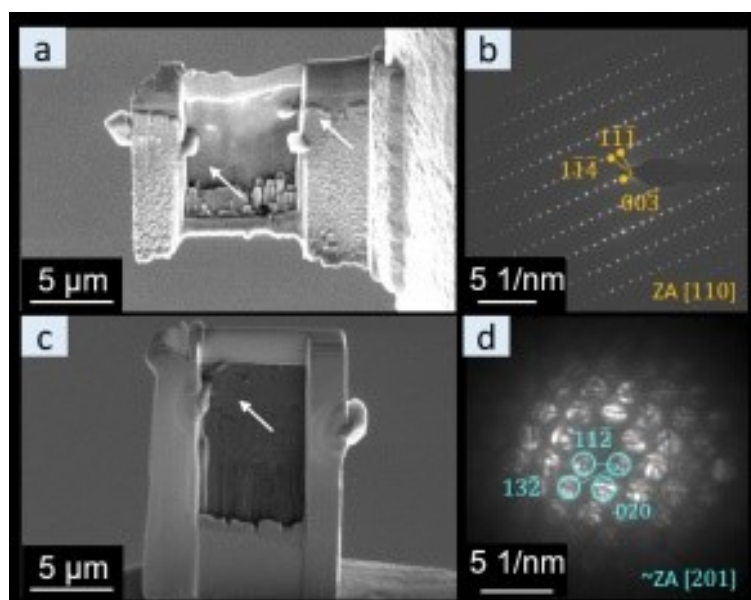


Figure 3. s-FIB fabricated TEM lamellas of BASE and NaSICON; a-d. HAADF-STEM image and EDS net intensity maps of Na, O and Al of BASE, e-h. HAADF-STEM image and EDS maps of the integrated intensity for Na, O and Si of NaSICON.

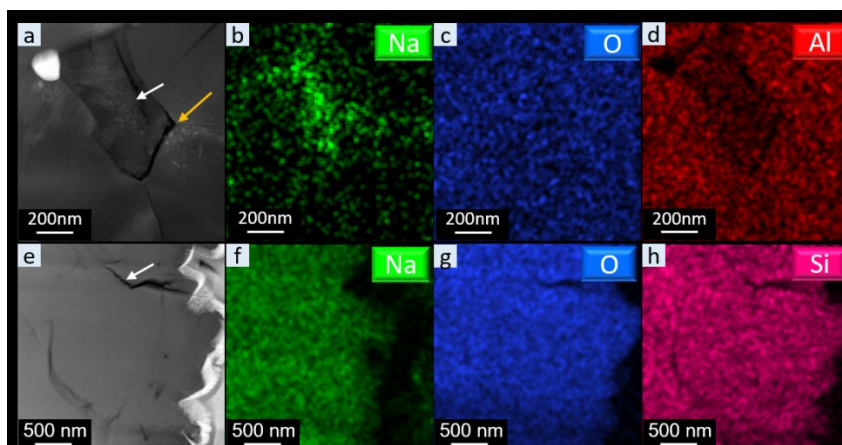


Figure 4. EDS spectra of different FIB fabricated BASE (a) and NaSICON samples (b).

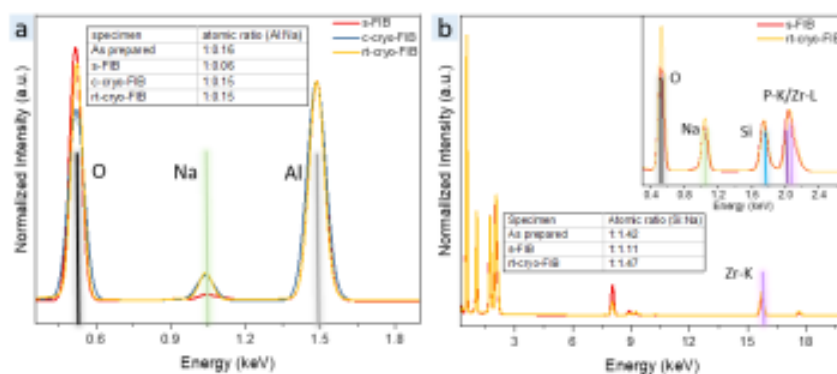


Figure 5. rt-cryo-FIB fabricated TEM lamellas of BASE and NaSICON; a-d. HAADF-STEM image and low dose EDS net intensity maps of Na, O, and Al of BASE; e-h. HAADF-STEM image and low dose EDS net intensity maps of Na, O, and Si of NaSICON.

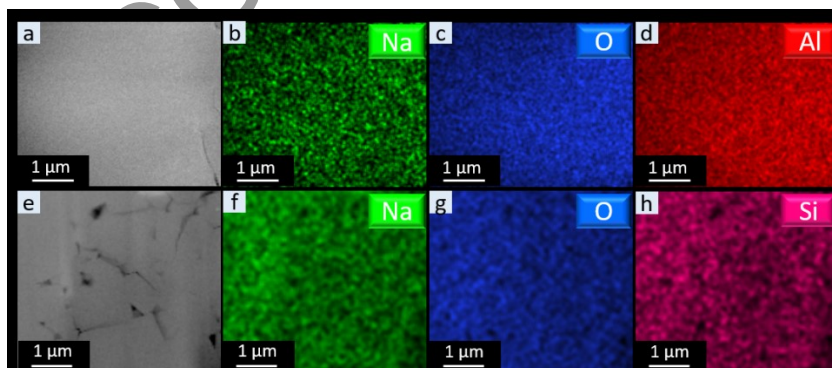


Figure 6. SEM imaging at 2 kV of a LiPON thin film with increasing dose and corresponding simplified model of the processes in the SEM: a. initial thin film morphology; b. after 22 e/nm^2 ; c. after 433 e/nm^2 ; d. after 995 e/nm^2 ; e. de-magnified SEM image after 3500 e/nm^2 ; f. simplified model of the structural changes observed with increasing dose in the SEM.

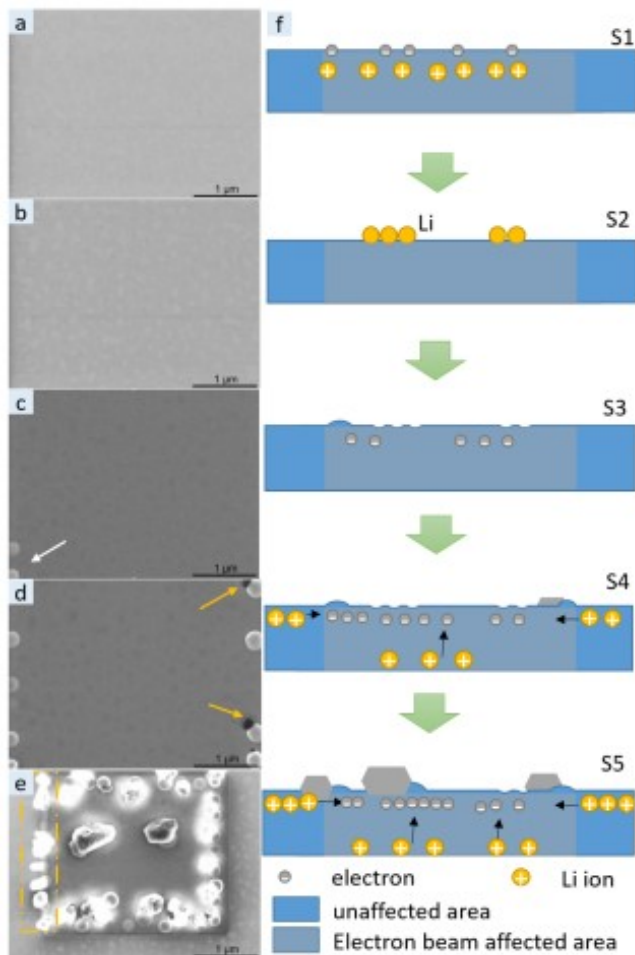


Figure 7. SEM imaging of a LiPON thin film at different acceleration voltages after applying a total dose of 3500 e/nm^2 to the blue rectangular region. At low voltages, some drift was unavoidable; a. 0.5 kV; b. 1 kV; c. 2 kV; d. 3 kV; e. 5 kV; f. 10 kV; g. 15 kV; h. 20 kV; i. 30 kV.

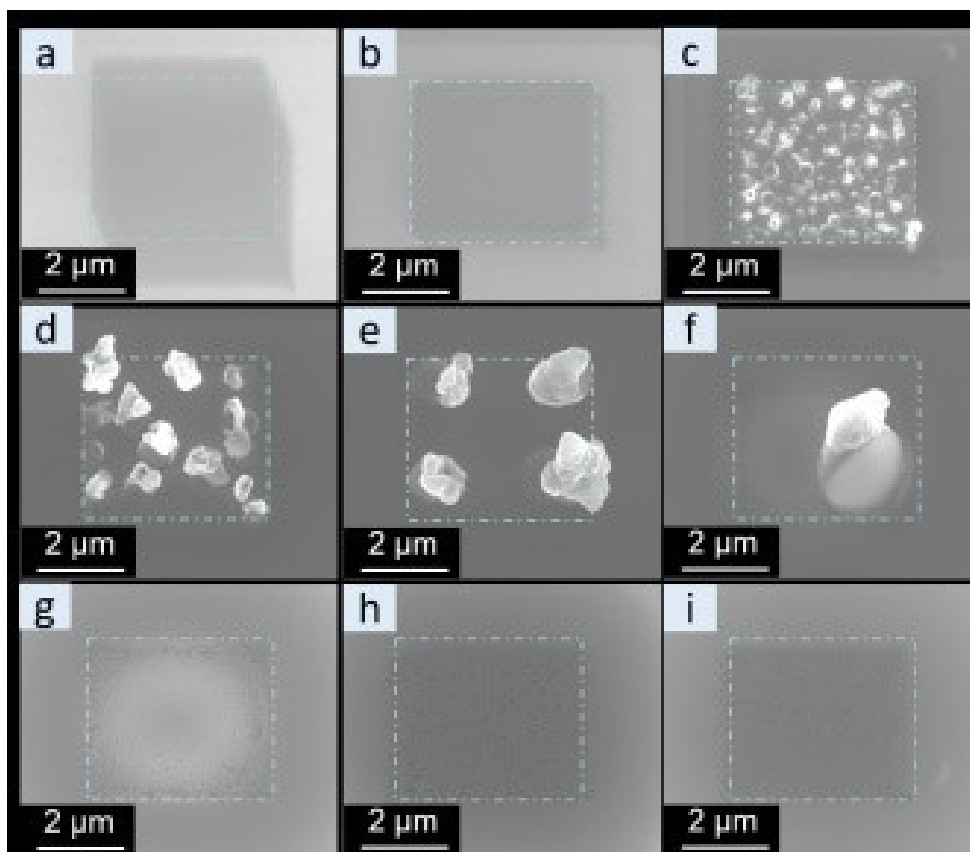
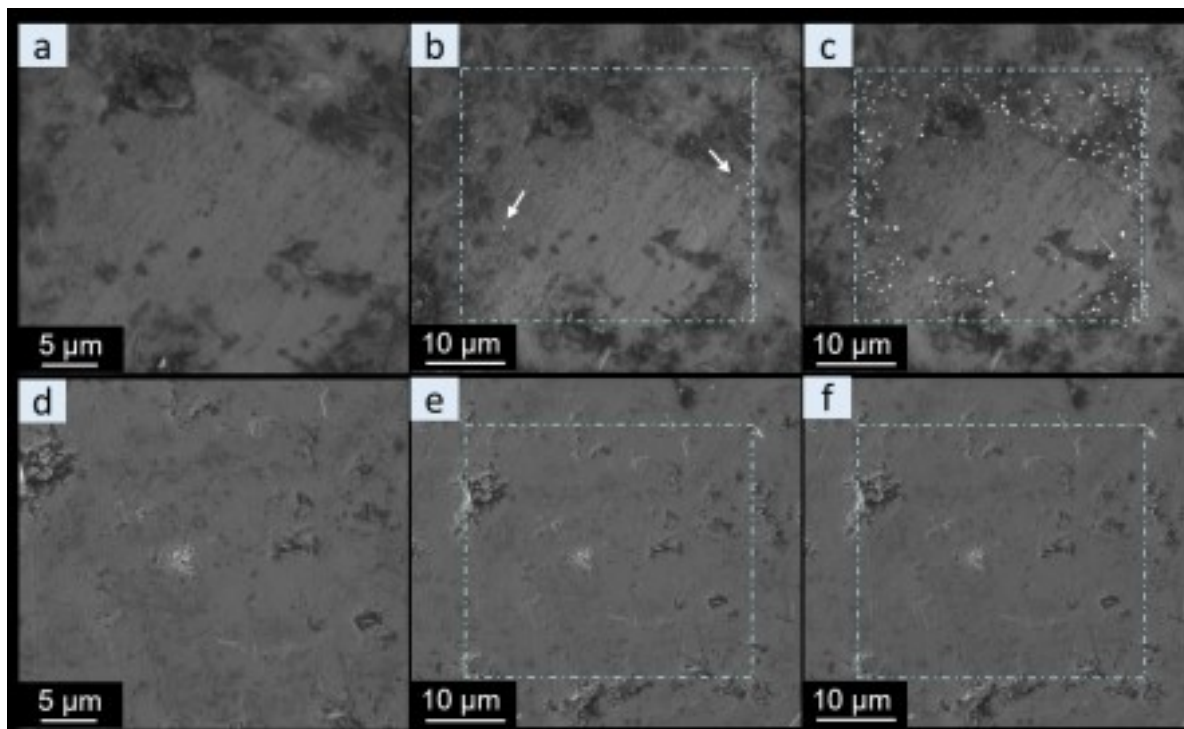


Figure 8. SEM images acquired at an acceleration voltage of 5 kV of pristine (a-c) and Au-coated (d-f) BASE pellets after exposure of the blue rectangular regions to different electron dose: a. pristine sample surface; b. first Na whisker growth (indicated by the white arrows) at a total dose of $\sim 600 \text{ e/nm}^2$; c. significantly increased growth of Na whiskers at the edge of the scanned region at a total dose of $\sim 1200 \text{ e/nm}^2$; d. pristine Au-coated BASE pellet; e. no whisker growth at a total dose of $\sim 600 \text{ e/nm}^2$; and f. $\sim 1200 \text{ e/nm}^2$.



ACCEPTED MANUSCRIPT